

# Demonstration of weighted graph optimization on a Rydberg atom array using local light-shifts

A. G. de Oliveira,<sup>1,\*</sup> E. Diamond-Hitchcock,<sup>1</sup> D. M. Walker,<sup>1</sup> M. T. Wells-Pestell,<sup>1</sup> G. Pelegrí,<sup>1</sup> C.J. Picken,<sup>2</sup> G.P.A. Malcolm,<sup>2</sup> A. J. Daley,<sup>1</sup> J. Bass,<sup>1</sup> and J. D. Pritchard<sup>1,†</sup>

<sup>1</sup>*Department of Physics and SUPA, University of Strathclyde, Glasgow G4 0NG, UK*

<sup>2</sup>*M Squared Lasers Limited, 1 Kelvin Campus, West of Scotland Science Park, Glasgow, G20 0SP, UK*

Neutral atom arrays have emerged as a versatile platform towards scalable quantum computation and optimization. In this paper we present first demonstrations of weighted graph optimization on a Rydberg atom array using annealing with local light-shifts. We verify the ability to prepare weighted graphs in 1D and 2D arrays, including embedding a five vertex non-unit disk graph using nine physical qubits and demonstration of a simple crossing gadget. We find common annealing ramps leading to preparation of the target ground state robustly over a substantial range of different graph weightings. This work provides a route to exploring large-scale optimization of non-planar weighted graphs relevant for solving relevant real-world problems.

Optimization of combinatorially hard problems has been identified as an early potential application of quantum computing hardware [1], with significant effort invested in developing protocols such as quantum annealing algorithms (QAA) [2–5] or variational based approaches such as Quantum Approximate Optimization Algorithms [6, 7]. Despite these efforts, hardware capable of demonstrating a practical quantum advantage in this domain remains elusive [8–11].

Neutral atom quantum computers based on arrays of individual optical tweezers [12–15] provide a scalable and versatile platform for quantum computing, with the ability to generate arrays of over 1000 qubits [16–19] and perform high-fidelity single- [20] and two-qubit [21–23] gate operations, enabling realization of small scale quantum algorithms [24]. This can be extended to implementation of logical qubit operations [25] by exploiting dynamical qubit reconfiguration [26]. Alongside digital operations, neutral atom arrays provide access to programmable spin models for performing quantum simulation [27] enabling exploration of phase diagrams and dynamics in 1D [28] and 2D [29, 30] and observation of novel topological phenomena [31, 32].

The ability to implement programmable spin models extends the utility of neutral atom arrays to the regime of analogue quantum computing [33, 34], where in the context of graph optimization coupling atoms to the Rydberg states enables native embedding of the Maximum Independent Set (MIS) problem for planar 2D unit-disk graphs (UDG) [35, 36]. Here the Rydberg blockade mechanism [37] prevents more than a single Rydberg excitation occurring within a radius  $r < r_B$ , enforcing the constraint that no two connected vertices should be simultaneously part of the same MIS configuration. Experimental demonstrations of solving MIS on 2D-UDG using QAA with hundreds of qubits demonstrate the feasibility of this approach [38, 39], however recent analysis shows for the native Kings-graph classical solvers are able to find solutions to graphs with 1000 vertices in minutes [40]. One approach for extending beyond planar 2D graph is to use ancillary qubits to create quantum wires [41] which can be routed through neighboring trapping planes in 3D to implement non-local graph connectivity [42]. This approach has been used to demonstrate embedded integer factor-

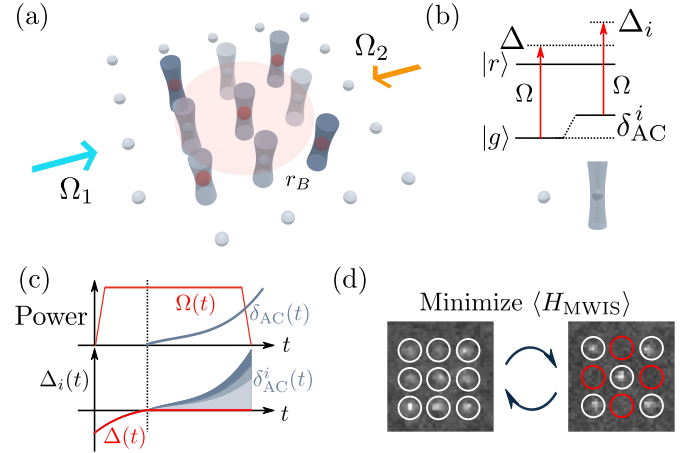


FIG. 1. Weighted graph optimization with local light-shifts. (a) The target graph problem is embedded onto a neutral atom array as a Maximum Weighted Independent Set (MWIS) on a Unit Disk Graph (UDG), using global Rydberg excitation lasers ( $\Omega_{1,2}$ ) and an additional set of tweezer beams for implementing local light-shifts with a programmable shift on each qubit site. The Rydberg blockade mechanism prevents two atoms within distance  $r_B$  being simultaneously excited. (b) Atoms without light-shift experience an effective two-photon Rabi frequency  $\Omega$  and global detuning  $\Delta$ . The light-shift tweezers induce AC shift  $\delta_{AC}^i = w_i \delta_{AC}$  on atom  $i$  to implement a local detuning  $\Delta_i = \Delta + \delta_{AC}^i$  with relative weight  $w_i$ . (c) Annealing protocol using a two-stage process with the global Rydberg laser ramped from an initial negative  $\Delta$  to resonance, then positive detunings defined by controlling power in light-shift tweezers to scale  $\delta_{AC}$  resulting in local detunings with fixed relative ratios defined by weightings  $w_i$ . (d) Ground-state solutions obtained via closed-loop optimization of the annealing profile to minimize the expectation value of the classical MWIS cost function.

ization [43] and quadratic unconstrained binary optimization (QUBO) problems [44] onto atom arrays using only global control.

Another approach to extend the range of problems that can be encoded using neutral atom arrays is to introduce local control fields as initially proposed in [45]. This permits the introduction of weighting to enable solution of Maximum Weighted Independent Set (MWIS) problems on a 2D UDG,

providing a route to map a variety of graph and QUBO problems onto neutral atom arrays using this MWIS-UDG encoding [46] with at worst a quadratic overhead in physical qubit number. Similar scaling is obtained using a related parity-based encoding for graph problems [47]. Moving beyond the blockade regime to remove the UDG restriction offers prospects for a linear scaling in qubit overhead and application to MaxCut problems [45]. To date, local light-shifts have been used on neutral atom arrays in the field of quantum simulation for generating large-scale entangled states [48], implementing fast, arbitrary local control of interacting trimers [49] and studying quantum coarsening dynamics [50].

In this paper we present first demonstrations of weighted graph optimization on a Rydberg atom array using annealing with local light-shifts. Our approach for weighting combines holographic techniques for generating programmable local light-shifts compatible with use on an arbitrary array geometry with the ability to implement graph annealing using global laser control fields, simplifying the number of available parameters when performing optimization. We verify the ability to prepare weighted graphs on both 1D and 2D arrays, including embedding a 5-qubit non-UDG using 9 physical qubits. In each case we find a common annealing ramp able to prepare the target ground state solutions for arbitrary graph weightings. This work demonstrates the feasibility of implementing weighted optimization using neutral atom arrays, and provides a route to embedding non-planar graphs solving relevant real-world problems [51].

*Weighted Graph Optimization.*— The Maximum Weighted Independent Set (MWIS) problem on graph  $G(V, E)$  comprised of  $E$  edges and  $V$  vertices, each of weight  $w_i > 0$ , is defined as finding the subset of vertices offering the highest total summed weights whilst ensuring that no pair of adjacent vertices (i.e. connected by an edge) are included. Introducing the binary variables  $n_i = \{0, 1\}$  to indicate whether vertex  $i$  belongs to the MWIS set, the classical cost function that must be minimized to solve the MWIS problem is

$$H_{\text{MWIS}} = - \sum_{i \in V} w_i n_i + \sum_{(i,j) \in E} U_{ij} n_i n_j, \quad (1)$$

where  $U_{ij} > \max_k(w_k)$ . Here the first term rewards inclusion of high-weight vertices, whilst the second term acts to penalize inclusion of vertices connected by an edge. For the case that  $G$  is a UDG, this cost function can be natively mapped to the case of a neutral atom array which has the Hamiltonian given by

$$H_{\text{Ryd}} = \sum_i \left( \frac{\Omega}{2} \sigma_i^x - \Delta_i \hat{n}_i \right) + \sum_{j>i} V(|\mathbf{r}_i - \mathbf{r}_j|) \hat{n}_i \hat{n}_j, \quad (2)$$

where  $\Omega$  is the Rabi frequency,  $\sigma_i^x = |r\rangle_i \langle g| + |g\rangle_i \langle r|$ ,  $\Delta_i$  is a site dependent detuning,  $\hat{n}_i = |r\rangle_i \langle r|$  is the projector onto the Rydberg state of atom  $i$ ,  $\mathbf{r}_i$  is a position vector and  $V(r) = C_6/r^6$  is the dipole-dipole interaction strength between two atoms. In the limit  $\Omega = 0$ , the ground state of  $H_{\text{Ryd}}$  encodes the solution to the MWIS problem if  $\Delta_i = w_i$

and  $V(|\mathbf{r}_i - \mathbf{r}_j|) > \max_k(w_k)$  for all  $i, j$  sharing an edge, enabling solution of UDG-MWIS problems by annealing atoms to the ground state configuration [46].

For arbitrary problems, such as non-UDG graphs or QUBO, the graph (and associated constraints) must first be encoded into a weighted UDG-MWIS. Ref. [46] provides one approach to implementing this mapping by introducing regular sub-graph gadgets to realize arbitrary non-local connections between vertices, however the focus of this present work is to verify the experimental feasibility for preparing the MWIS on a neutral atom array.

*MWIS Annealing Protocol.*— Starting with a target MWIS graph problem, the graph is first mapped to a UDG-MWIS which can be geometrically embedded onto a neutral atom array using techniques from [46] with a spacing  $a$  between neighbouring atoms chosen to be below the blockade radius  $r_B$  to ensure the blockade constraint is realized. Graph weighting is implemented with an additional light-shifting potential that is holographically projected onto the atoms using a spatial light modulator (SLM) to apply local light-shifts with arbitrary geometry and programmable relative weighting. These additional tweezer beams, shown schematically in Fig. 1, cause a differential AC Stark shift  $\delta_{\text{AC}}^i$  on each atom proportional to the relative power in each tweezer, resulting in a total shift  $\Delta_i = \Delta + \delta_{\text{AC}}^i$ , where  $\Delta$  is the detuning of the global Rydberg lasers used to realize a homogeneous two-photon coupling between ground and Rydberg states. In the experiments below, the light-shift laser is blue-detuned for both ground and Rydberg states, ensuring that  $\delta_{\text{AC}}^i \geq 0$  as required. For a given graph weighting, the relative light-shifts are calibrated to realize  $\delta_{\text{AC}}^i = w_i \delta_{\text{AC}}$ , where  $\delta_{\text{AC}}$  is the global unit scale ( $w = 1$ ) of the light-shift and  $w_i$  are the relative weights of the embedded graph problem. To avoid violating the blockade condition, it is necessary to constrain the maximum value of  $\delta_{\text{AC}}$  such that  $\max_i(\delta_{\text{AC}}^i) < V(a)$ , where  $a$  is the interatomic spacing.

To adiabatically prepare atoms in the ground state encoding the solution of the UDG-MWIS problem, a cubic detuning profile is used [52], as illustrated in Fig. 1(c). Starting with the atoms initially prepared in  $|g\rangle$ , the global Rabi frequency  $\Omega$  is ramped up using a fixed negative detuning after which the detuning is swept towards resonance. Once the global detuning reaches resonance,  $\Delta = 0$ , the global detuning is held fixed and the remaining detuning profile is applied by dynamically varying the intensity of the light-shifting potential to control  $\delta_{\text{AC}}(t)$ . By deriving the local light-shifts from a single laser, it is possible to use global intensity control for implementing arbitrary detuning ramps whilst maintaining fixed relative weightings on the graph. The Rabi frequency  $\Omega$  is then ramped off whilst maintaining the light-shift, after which the encoded bitstrings  $\{n_i\}$  are read out by fluorescence imaging. Atoms excited to the Rydberg state are ejected from the trap, whilst atoms in the ground state survive and appear in the images. Using a closed-loop optimization process, the cubic ramp parameters are adjusted to minimize the classical cost function  $\langle H_{\text{MWIS}} \rangle$  to maximize the probability of preparing

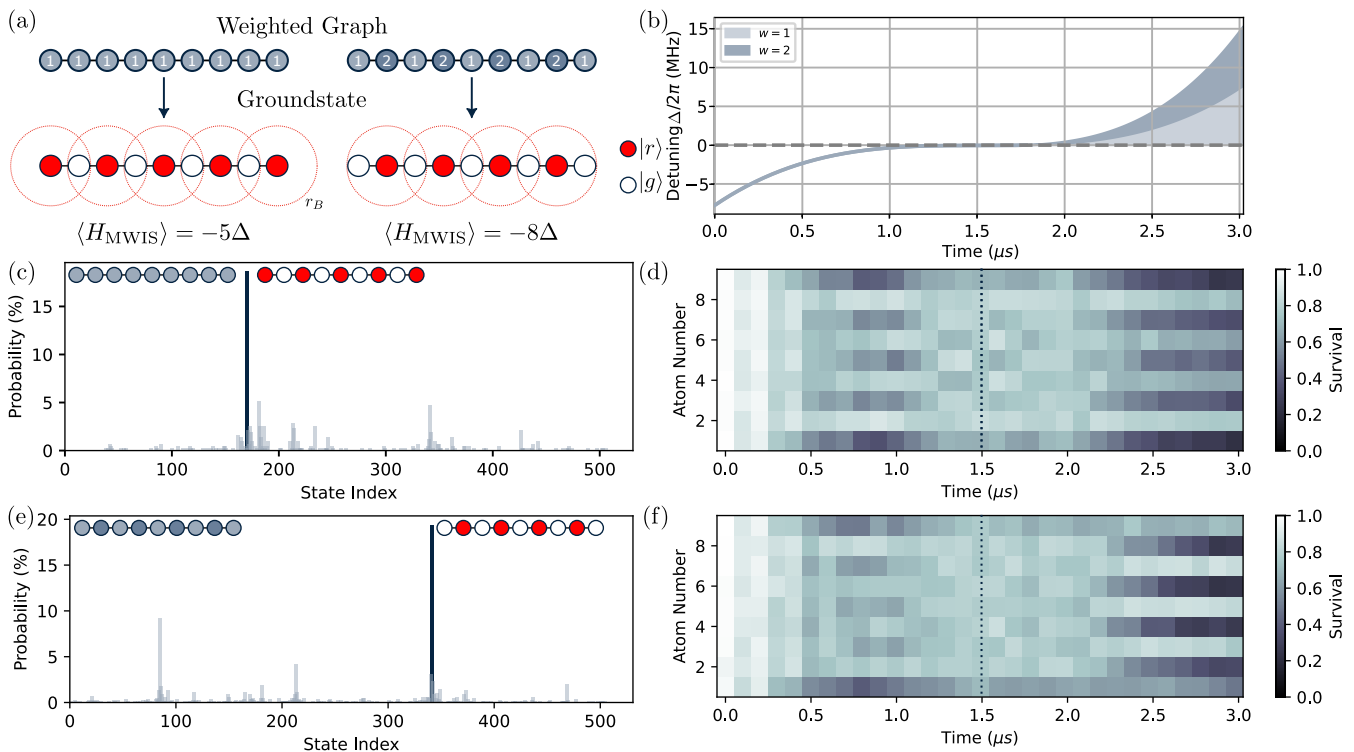


FIG. 2. 1D Weighted Graphs. (a) For a uniformly weighted, odd-length 1D graph the ground state is the  $Z_2$ -ordered phase with Rydberg excitations on odd sites which corresponds to the unweighted MIS. Introducing a weighting with  $w_i = 2$  on even sites results in an MWIS ground state with Rydberg excitations localized to the even sites which is no longer equivalent to the MIS solution. (b) Optimal annealing ramp for preparing the weighted ground state obtained via closed-loop optimization for  $N = 9$  atoms spaced by  $a = 7 \mu\text{m}$ . Output state probability (c) and time evolution (d) for the unweighted graph showing the odd-ordered target ground state is prepared with 19(1)% probability. Output state probability (e) and time evolution (f) for the weighted graph showing even-ordered ground state is also prepared with 19(1)% probability.

the system in the MWIS ground state, as shown in Fig. 1(d). Following this optimization process, the solution of the target MWIS graph problem can then be determined from the most probable output bitstrings.

*Experimental Setup.*— The experimental setup is based on arrays of holographically trapped Cs atoms. Atoms are initially prepared in the  $|g\rangle = |4, 0\rangle$  state, and are globally excited to the  $|r\rangle = |80s_{1/2}, m_j = +1/2\rangle$  Rydberg state via two-photon excitation using the  $7p_{1/2}$  intermediate state using light at 459 nm and 1039 nm. We operate with a detuning of  $\Delta'/2\pi = 502$  MHz from the intermediate state, and achieve a Rydberg Rabi frequency of  $\Omega/2\pi = 2.70(2)$  MHz. Global detuning is controlled by adjusting the frequency using a double-passed acousto-optic modulator (AOM) in the 459 nm path. For  $80s_{1/2}$  we calculate  $C_6 = -3376 \text{ GHz } \mu\text{m}^6$  [53], resulting in a resonant blockade radius  $r_B = \sqrt[6]{|C_6|/\Omega} = 10.4 \mu\text{m}$ .

Local light-shifts are realized using light at 800 nm derived from a Ti:Sapph laser that is projected from a spatial light modulator (SLM) and overlapped with the main optical trapping array. To suppress mechanical forces coming from the repulsive optical potential, the light-shift spot arrays are re-imaged onto the atoms with a  $1/e^2$  radius of  $3.0(4) \mu\text{m}$ . For a given UDG-MWIS, the arrays of local light-shift beams are

generated using a Gerchberg-Saxon algorithm with the desired relative weighting [54]. To verify the light-shifts experienced by the atoms, we perform spectroscopy on the  $|g\rangle \rightarrow |50s_{1/2}, m_j = +1/2\rangle$  transition to suppress interactions, and perform a closed-loop feedback on the SLM potentials to achieve target weightings with  $< 2\%$  RMS errors in the relative weightings after 5 iterations [52]. The resulting differential light-shift is calibrated as  $\delta_{\text{AC}} = 0.28(2)$  MHz/mW, which is dominated by the ground state light-shift as the Rydberg AC shift calculated using the polarizability of a free electron corresponds to only 40 kHz [55].

*1D Weighted Graphs.*— As an artificial first demonstration of the feasibility to perform weighted optimization using the dual-stage protocol defined above, we begin with a simple and well studied problem of a 1D weighted graph as illustrated in Fig. 2(a). For a uniformly weighted set of  $N$  atoms with  $w_i = 1$  spaced such that  $a < r_B < 2a$ , for odd  $N$  the ground state corresponds to a  $Z_2$  ordered phase with Rydberg excitations localized on the odd sites as previously observed using global control only [28]. Introducing a relative weighting of  $w_i = 2$  on the even sites results in a modification of the MWIS ground state to prepare the inverted output string with Rydberg excitations now localized to the even sites.

We perform experiments on weighted 1D graphs using two

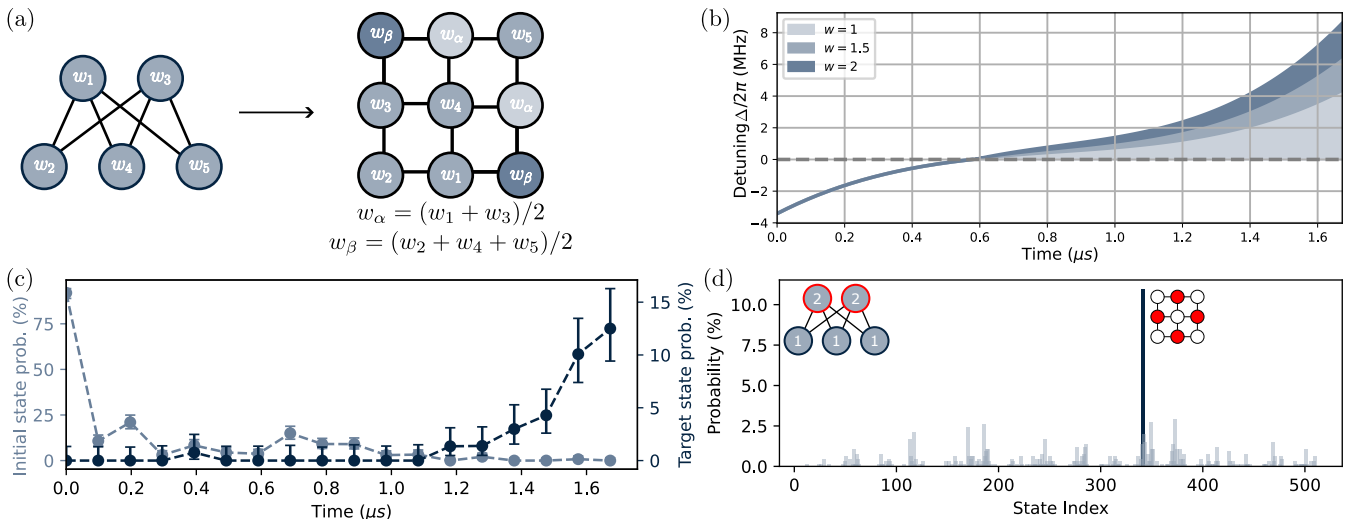


FIG. 3. 2D Weighted Graphs (a) Target graph is a 5 vertex non-UDG MWIS, which can be mapped to the 9 atom UDG-MWIS graph [46] by introducing four ancilla qubits with weightings  $w_\alpha$  and  $w_\beta$  to implement the edges from vertex 5 to vertices 1 and 3. (b) Optimized annealing profile for the graph instance with  $(w_1, w_2, w_3, w_4, w_5) = (2, 1, 2, 1, 1)$  which results in  $\langle H_{\text{MWIS}} \rangle = -4.0(1)$ , compared to the idealized cost of  $-8$ . (c) Time-evolution data for the weighted graph showing adiabatic evolution during the ramp to reach the correct target state. (d) Final output state probability distribution from 1000 experimental realizations showing the correct MWIS solution is observed with 11(1)% probability, with all other output strings observed with  $\leq 2.5\%$  probability.

20  $\mu\text{m}$  separated parallel lines of  $N = 9$  atoms spaced by  $a = 7 \mu\text{m}$ , with one row set to have uniform light-shifts and the second row having  $w_i = 2$  on the even sites. Starting with a linear profile, we apply the global light-shift on both graphs simultaneously, and perform closed-loop feedback to minimize  $\langle H_{\text{MWIS}} \rangle$  for the weighted graph using the classical cost function defined in Eq. 1. Whilst encoding the same effective ground state energy as  $H_{\text{Ryd}}$ , using the classical cost function avoids issues with the optimizer trivially driving the system to large negative detunings  $\Delta_i$  as a route to further minimising the energy of the observed output configurations. The resulting optimized profile is shown in Fig. 2(b), corresponding to a duration of 3  $\mu\text{s}$  with light-shifts turned on from 1.5  $\mu\text{s}$  when the global Rydberg laser detuning reaches zero.

The resulting distributions of output strings are shown for both uniform and weighted graphs in Fig. 2(c,e) respectively. Using a common annealing profile, we observe the correct ground states as the most probable state outputs in both cases, with probabilities of 19(1)% in both cases. The additional 9% peak in Fig. 2(e) with state index 93 corresponds to the target output state with the first qubit also lost. This appears higher than other states due to slightly increased single atom loss measured for this array site. Time evolution data is shown for each graph in Fig. 2(d,f) respectively, which clearly demonstrates the adiabatic nature of graph preparation at longer times and the emergence of the ground state ordering as expected.

*2D Weighted Graphs.*— Moving beyond the trivial 1D case, we consider the example of a non-UDG 2D MWIS shown in Fig. 3(a). This graph, featuring five vertices, has MWIS solutions corresponding to either qubits 1 and 3 being excited, or

qubits 2, 4 and 5. To map this to a UDG-MWIS graph for implementation on our neutral atom array, we follow the protocol of Ref. [46] resulting in a 9-qubit graph requiring four ancilla qubits to implement the edges between vertices 1 and 2 and vertex 5. By symmetry this introduces two additional weightings,  $w_\alpha$  and  $w_\beta$  on the ancilla qubits. We use the weightings  $w_\alpha = (w_1 + w_3)/2$  and  $w_\beta = (w_2 + w_4 + w_5)/2$  which guarantees that for any arbitrary weighting with  $w_i > 0$  we realize the MWIS solution as the ground state of the Rydberg interaction Hamiltonian.

Initially we consider the weighted graph instance indicated by the inset of Fig. 3(d) with  $(w_1, w_2, w_3, w_4, w_5) = (2, 1, 2, 1, 1)$  using a  $3 \times 3$  arrangement of atoms with spacing  $a = 8 \mu\text{m}$ . As before, we perform closed-loop optimization of the annealing profile, resulting in a shorter annealing time of only 1.65  $\mu\text{s}$  with the light-shift turning on after 0.6  $\mu\text{s}$ , as shown in Fig. 3(b). For this optimization process we minimize  $\langle H_{\text{MWIS}} \rangle$  for the embedded 9 qubit graph (rather than simply just considering the non-embedded 5-qubit graph), as whilst the values of the ancilla qubits are not relevant to the problem solution, there are many possible states encoded in the 9-qubit bitstrings that feature the correct 5-vertex solution state but only one of which corresponds to the energetic ground state. This ensures the optimizer favours solutions that more closely follow adiabatic preparation of the ground states, which can be verified by observing the dynamical evolution in preparing the correct output bitstring. Fig. 3(c) shows the preparation probability as a function of time, revealing a smooth accumulation of population after 1.2  $\mu\text{s}$  and no fast oscillations observed when exploiting shorter annealing profile durations. Following optimization of ramp parameters we obtain

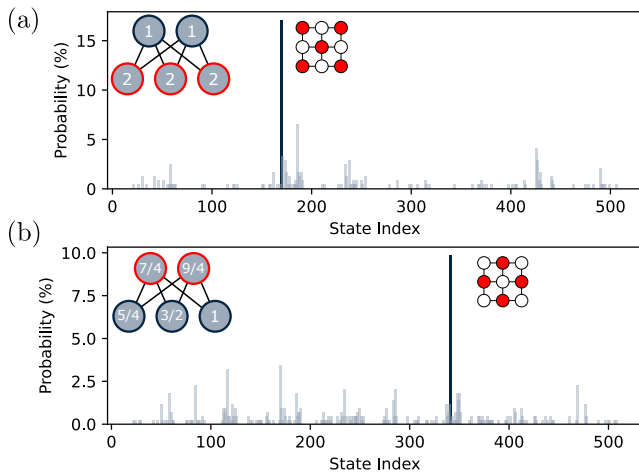


FIG. 4. Annealing alternative graph instances. We use the optimised ramp found on the  $(2, 1, 2, 1, 1)$  graph and apply it to (a)  $(1, 2, 1, 2, 2)$  and (b)  $(7/4, 5/4, 9/4, 3/2, 1)$  graph instances. In both cases, the ramp provides the correct solution to the MWIS graph even for the case of the inverted ground state for (a), resulting in target state output probabilities of 17(2)% and 10(1)% with  $\langle H_{\text{MWIS}} \rangle = -6.9(2)$  and  $-3.5(1)$  respectively.

$\langle H_{\text{MWIS}} \rangle = -4.0(1)$ , compared to an idealized cost of -8.

The final output state probabilities for the weighted graph are shown in Fig. 3(d), with the correct 9-qubit output state corresponding to Rydberg excitation of qubits mapping onto vertices 1 and 3 being observed with  $\geq 10\%$  probability, significantly higher than any other output bitstrings and showing demonstration of solving an embedded MWIS graph.

One further advantage of identifying an adiabatic annealing profile is that it should be robust against changes in graph weightings. To verify this for the graph shown in Fig. 3, we directly implement the same annealing profile but with different relative weightings of  $(1, 2, 1, 2, 2)$  and  $(7/4, 5/4, 9/4, 3/2, 1)$ . The results are shown in Fig. 4 where for both cases the annealing process is able to prepare the system in the correct ground state, even for Fig. 4(a) which corresponds to the inverted solution state to that targeted previously to optimize the original annealing profile.

*Gadgets.*— As discussed above, a number of proposals exist to extend the range of target optimisation problems that can be solved using neutral atom arrays by converting to a UDG-MWIS [45–47]. One such approach introduces simple *gadgets* that provide a generalised framework for mapping problems to UDG-MWIS [46], and here we consider a proof-of-concept implementation of the crossing gadget using our local light-shift approach. This crossing gadget, shown in Fig. 5(a), implements an edge between qubits 1 and 2, and qubits 3 and 4. This requires four additional atoms, where the logical qubits (1-4) are assigned weight  $w_1 = 1$ , whilst the ancilla gadgets have  $w_2 = 2.86$  to ensure the lowest energy state corresponds to an equal superposition of the four degenerate output configurations with either qubit 1 or 2 excited independent of 3 or 4. This deviates from  $w_2 = 4$

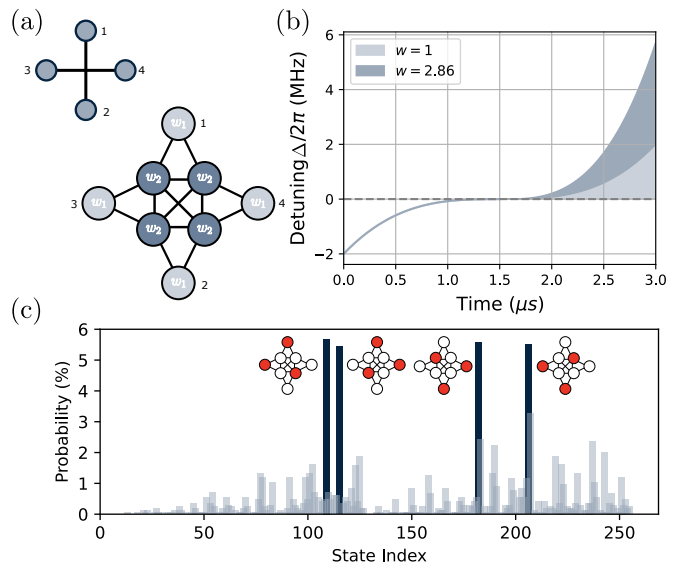


FIG. 5. Crossing gadget. (a) Crossing gadget designed to enable logical crossing of two quantum wires connecting qubits 1 and 2, and 3 and 4, without introducing coupling between them. To compensate for interaction tails we use  $w_1 = 1$  for logical qubits and  $w_2 = 2.86$  for the ancilla atoms. The spacing between two adjacent sites with  $w_2$  is  $6 \mu\text{m}$ , and  $7.5 \mu\text{m}$  between them and their nearest  $w_1$  neighbour. (b) Optimized annealing ramp (c) Final gadget output strings showing the four degenerate ground states are each prepared with probabilities of 5(1)%.

presented in [46] due to the requirement to compensate for the effects of the  $1/R^6$  interaction tails on the ancilla atoms. For these measurements the intermediate state detuning was increased to  $\Delta'/2\pi = 1 \text{ GHz}$  and Rabi frequency reduced to  $\Omega/2\pi = 1.28 \text{ MHz}$  motivated by numerical modelling of the annealing process. As above, we then optimize the annealing ramp experimentally to minimize  $\langle H_{\text{MWIS}} \rangle$  for the problem resulting in the ramp shown in Fig. 5(b). The distribution of the final output strings are shown in Fig. 5(c), where the four target ground states are the most likely to be observed with approximately equal probability, and  $\geq 20\%$  combined probability. Analysis of the next four most probable output strings show these correspond to the case of a target ground state with one of the logical qubit Rydberg excitation's missing, likely due to limitations in the Rydberg detection fidelity. For embedding of larger graphs, improvements in the Rydberg state detection can be implemented using microwave ionization [29, 56], however these results verify the proof-of-concept approach for performing gadget encodings on the current architecture.

*Discussion and Outlook.*— In this paper we have demonstrated a new approach to implementing UDG-MWIS using arbitrary local light-shifts implemented using a SLM combined with a dual stage annealing profile that combines the advantages of local light-shifts with global frequency and intensity control for implementing a quantum annealing algorithm. We demonstrate the ability to prepare ground states of small-scale 1D and 2D graphs, including demonstrating the

embedding of a non-UDG MWIS problem. In both cases, we were able to identify robust annealing protocols suitable for use with different relative weightings providing the possibility to design universal ramps that are suitable for solving a large number of graphs without the required overhead of full closed-loop optimization of the annealing ramp each time.

This approach for local light-shifts is highly scalable, with SLMs able to generate arrays of  $>1000$  individually controllable spots and the option to implement in-situ realtime feedback using a camera calibrated against the measured atomic shift previously demonstrated for normalization of arbitrary trapping potentials [25]. Currently at 800 nm we have up to 4 W available at the experiment, providing sufficient power for  $>100$  weighted sites. In future, this can be scaled further using coherent combination or frequency doubling telecoms fiber lasers to increase the available power and combined with techniques for beam-shaping to implement a flat-top point spread function on the SLM [57] to reduce the size of the light-shift spots and further reduce mechanical effects caused by using a repulsive optical potential to enable longer annealing runs.

For larger graph problems, the quadratic overhead introduced by the UDG-MWIS encoding [46] introduces interesting open questions around scalability of this approach, whilst recent theoretical work exploring annealing of unweighted graph shows even for relatively simple graph constructions it is possible to have minimum energy gaps that decay super-exponentially with system size [58] requiring use of optimal control techniques or quenches to prepare atoms in the target ground states. In future work we will explore this question further, and provide a comparison against other encoding protocols requiring local light-shifts as a route to identifying useful applications of weighted graph optimization on neutral atom arrays [45, 47].

We thank H. Pichler for helpful discussions. This work is supported by the EPSRC Prosperity Partnership *SQuAre* (Grant No. EP/T005386/1) with funding from M Squared Lasers Ltd and EPSRC Grant EP/Y005058/2. The data presented in this work are available at [59].

\* andre.oliveira@strath.ac.uk

† jonathan.pritchard@strath.ac.uk

- [1] A. Abbas, A. Ambainis, B. Augustino, A. Bärttschi, H. Buhrman, C. Coffrin, G. Cortiana, V. Dunjko, D. J. Egger, B. G. Elmegreen, N. Franco, F. Fratini, B. Fuller, J. Gacon, C. Gonciulea, S. Gribling, S. Gupta, S. Hadfield, R. Heese, G. Kircher, T. Kleinert, T. Koch, G. Korpas, S. Lenk, J. Marecek, V. Markov, G. Mazzola, S. Mensa, N. Mohseni, G. Nannicini, C. O’Meara, E. P. Tapia, S. Pokutta, M. Proissl, P. Rebentrost, E. Sahin, B. C. B. Symons, S. Tornow, V. Valls, S. Woerner, M. L. Wolf-Bauwens, J. Yard, S. Yarkoni, D. Zechiel, S. Zhuk, and C. Zoufal, arXiv:2312.02279 [quant-ph] (2023).
- [2] E. Farhi, J. Goldstone, S. Gutmann, and M. Sipser, arXiv:quant-ph/0001106 [quant-ph] (2000).
- [3] E. Farhi, J. Goldstone, S. Gutmann, J. Lapan, A. Lundgren, and D. Preda, *Science* **292**, 472 (2001).
- [4] G. E. Santoro and E. Tosatti, *J. Phys. A* **39**, R393 (2006).
- [5] T. Albash and D. A. Lidar, *Rev. Mod. Phys.* **90**, 015002 (2018).
- [6] E. Farhi, J. Goldstone, and S. Gutmann, 1411.4028 [quant-ph] (2014).
- [7] L. Zhou, S.-T. Wang, S. Choi, H. Pichler, and M. D. Lukin, *Phys. Rev. X* **10**, 021067 (2020).
- [8] G. G. Guerreschi and A. Y. Matsuura, *Scientific Reports* **9**, 6903 (2019).
- [9] D. Lykov, J. Wurtz, C. Poole, M. Saffman, T. Noel, and Y. Alexeev, *npj Quantum Information* **9**, 73 (2023).
- [10] R. Shaydulin, C. Li, S. Chakrabarti, M. DeCross, D. Herman, N. Kumar, J. Larson, D. Lykov, P. Minssen, Y. Sun, Y. Alexeev, J. M. Dreiling, J. P. Gaebler, T. M. Gatterman, J. A. Gerber, K. Gilmore, D. Gresh, N. Hewitt, C. V. Horst, S. Hu, J. Johansen, M. Matheny, T. Mengle, M. Mills, S. A. Moses, B. Neyenhuis, P. Siegfried, R. Yalovetzky, and M. Pistoia, *Science Adv.* **10**, eadm6761 (2023).
- [11] H. M. Bauza and D. A. Lidar, arXiv:2401.07184 [quant-ph] (2024).
- [12] M. Saffman, *J. Phys. B* **49**, 202001 (2016).
- [13] L. Henriot, L. Beguin, A. Signoles, T. Lahaye, A. Browaeys, G.-O. Reymond, and C. Jurczak, *Quantum* **4**, 327 (2020).
- [14] J.-L. Wu, Y. Wang, J.-X. Han, S.-L. Su, Y. Xia, Y. Jiang, and J. Song, *Phys. Rev. A* **103**, 012601 (2021).
- [15] M. Morgado and S. Whitlock, *AVS Quantum Science* **3**, 023501 (2021).
- [16] P. Huft, Y. Song, T. M. Graham, K. Jooya, S. Deshpande, C. Fang, M. Kats, and M. Saffman, *Phys. Rev. A* **105**, 063111 (2022).
- [17] M. A. Norcia, H. Kim, W. B. Cairncross, M. Stone, A. Ryou, M. Jaffe, M. O. Brown, K. Barnes, P. Battaglino, T. C. Bohdanowicz, A. Brown, K. Cassella, C. A. Chen, R. Coxe, D. Crow, J. Epstein, C. Griger, E. Halperin, F. Hummel, A. M. W. Jones, J. M. Kindem, J. King, K. Kotru, J. Lauigan, M. Li, M. Lu, E. Megidish, J. Marjanovic, M. McDonald, T. Mittiga, J. A. Muniz, S. Narayanaswami, C. Nishiguchi, T. Paule, K. A. Pawlak, L. S. Peng, K. L. Pudenz, D. R. Perez, A. Smull, D. Stack, M. Urbanek, R. J. M. van de Veerdonk, Z. Vendeiro, L. Wadleigh, T. Wilkason, T. Y. Wu, X. Xie, E. Zalys-Geller, X. Zhang, and B. J. Bloom, arXiv:2401.16177 [quant-ph] (2024).
- [18] F. Gyger, M. Ammenwerth, R. Tao, H. Timme, S. Snigirev, I. Bloch, and J. Zeiher, arXiv:2402.04994 [quant-ph] (2024).
- [19] H. J. Manetsch, G. Nomura, E. Bataille, K. H. Leung, X. Lv, and M. Endres, arXiv:2403.12021 [quant-ph] (2024).
- [20] B. Nikolov, E. Diamond-Hitchcock, J. Bass, N. L. R. Spong, and J. D. Pritchard, *Phys. Rev. Lett.* **131**, 030602 (2023).
- [21] H. Levine, A. Keesling, G. Semeghini, A. Omran, T. T. Wang, S. Ebadi, H. Bernien, M. Greiner, V. Vuletić, H. Pichler, and M. D. Lukin, *Phys. Rev. Lett.* **123**, 170503 (2019).
- [22] S. J. Evered, D. Bluvstein, M. Kalinowski, S. Ebadi, T. Manovitz, H. Zhou, S. H. Li, A. A. Geim, T. T. Wang, N. Maskara, H. Levine, G. Semeghini, M. Greiner, V. Vuletić, and M. D. Lukin, *Nature* **622**, 268 (2023).
- [23] S. Ma, G. Liu, P. Peng, B. Zhang, S. Jandura, J. Claes, A. P. Burgers, G. Pupillo, S. Puri, and J. D. Thompson, *Nature* **622**, 279 (2023).
- [24] T. M. Graham, Y. Song, J. Scott, C. Poole, L. Phuttitarn, K. Jooya, P. Eichler, X. Jiang, A. Marra, B. Grinkemeyer, M. Kwon, M. Ebert, J. Cherek, M. T. Lichtman, M. Gillette, J. Gilbert, D. Bowman, T. Ballance, C. Campbell, E. D. Dahl, O. Crawford, N. S. Blunt, B. Rogers, T. Noel, and M. Saffman,

- Nature **604**, 457 (2022).
- [25] D. Bluvstein, S. J. Evered, A. A. Geim, S. H. Li, H. Zhou, T. Manovitz, S. Ebadi, M. Cain, M. Kalinowski, D. Hangleiter, J. P. Bonilla Ataides, N. Maskara, I. Cong, X. Gao, P. Sales Rodriguez, T. Karolyshyn, G. Semeghini, M. J. Gullans, M. Greiner, V. Vuletić, and M. D. Lukin, Nature **626**, 58 (2024).
- [26] D. Bluvstein, H. Levine, G. Semeghini, T. T. Wang, S. Ebadi, M. Kalinowski, A. Keesling, N. Maskara, H. Pichler, M. Greiner, V. Vuletić, and M. D. Lukin, Nature **604**, 451 (2022).
- [27] A. Browaeys and T. Lahaye, Nature Phys. **16**, 132 (2020).
- [28] H. Bernien, S. Schwartz, A. Keesling, H. Levine, A. Omran, H. Pichler, S. Choi, A. S. Zibrov, M. Endres, M. Greiner, V. Vuletić, and M. D. Lukin, Nature **551**, 579 (2017).
- [29] S. Ebadi, T. T. Wang, H. Levine, A. Keesling, G. Semeghini, A. Omran, D. Bluvstein, R. Samajdar, H. Pichler, W. W. Ho, S. Choi, S. Sachdev, M. Greiner, V. Vuletić, and M. D. Lukin, Nature **595**, 227 (2021).
- [30] P. Scholl, M. Schuler, H. J. Williams, A. A. Eberharter, D. Barredo, K.-N. Schymik, V. Lienhard, L.-P. Henry, T. C. Lang, T. Lahaye, A. M. Läuchli, and A. Browaeys, Nature **595**, 233 (2021).
- [31] S. de Léséleuc, V. Lienhard, P. Scholl, D. Barredo, S. Weber, N. Lang, H. Buchler, T. Lahaye, and A. Browaeys, Science **365**, 775 (2019).
- [32] G. Semeghini, H. Levine, A. Keesling, S. Ebadi, T. T. Wang, D. Bluvstein, R. Verresen, H. Pichler, M. Kalinowski, R. Samajdar, A. Omran, S. Sachdev, A. Vishwanath, M. Greiner, V. Vuletic, and M. D. Lukin, Science **374**, 1242 (2021).
- [33] M. Kim, J. Ahn, Y. Song, J. Moon, and H. Jeong, Journal of the Korean Physical Society **82**, 827 (2023).
- [34] C. Dalyac, L. Leclerc, L. Vignoli, M. Djellabi, W. da Silva Coelho, B. Ximenez, A. Dareau, D. Dreon, V. E. Elfving, A. Signoles, L.-P. Henry, and L. Henriët, arXiv:2403.11931 [quant-ph] (2024).
- [35] H. Pichler, S.-T. Wang, L. Zhou, S. Choi, and M. D. Lukin, 1808.10816 [quant-ph] (2018).
- [36] H. Pichler, S.-T. Wang, L. Zhou, S. Choi, and M. D. Lukin, 1809.04954 [quant-ph] (2018).
- [37] D. Jaksch, J. I. Cirac, P. Zoller, S. L. Rolston, R. Côté, and M. D. Lukin, Phys. Rev. Lett. **85**, 2208 (2000).
- [38] S. Ebadi, A. Keesling, M. Cain, T. T. Wang, H. Levine, D. Bluvstein, G. Semeghini, A. Omran, J.-G. Liu, R. Samajdar, X.-Z. Luo, B. Nash, X. Gao, B. Barak, E. Farhi, S. Sachdev, N. Gemelke, L. Zhou, S. Choi, H. Pichler, S.-T. Wang, M. Greiner, V. Vuletić, and M. D. Lukin, Science **376**, 1209 (2022).
- [39] K. Kim, M. Kim, J. Park, A. Byun, and J. Ahn, arXiv:2311.13803 [quant-ph] (2023).
- [40] R. S. Andrist, M. J. A. Schuetz, P. Minssen, R. Yalovetzky, S. Chakrabarti, D. Herman, N. Kumar, G. Salton, R. Shaydulin, Y. Sun, M. Pistoia, and H. G. Katzgraber, Phys. Rev. Res. **5**, 043277 (2023).
- [41] M. Kim, K. Kim, J. Hwang, E.-G. Moon, and J. Ahn, Nature Phys. **18**, 755 (2022).
- [42] C. Dalyac, L.-P. Henry, M. Kim, J. Ahn, and L. Henriët, arXiv:2306.13373 [quant-ph] (2023).
- [43] J. Park, S. Jeong, M. Kim, K. Kim, A. Byun, L. Vignoli, L.-P. Henry, L. Henriët, and J. Ahn, Phys. Rev. Res. **6**, 023241 (2024).
- [44] A. Byun, J. Jung, K. Kim, M. Kim, S. Jeong, H. Jeong, and J. Ahn, Adv. Quant. Tech. **7**, 2300398 (2024).
- [45] K. Goswami, R. Mukherjee, H. Ott, and P. Schmelcher, Phys. Rev. Res. **6**, 023031 (2024).
- [46] M.-T. Nguyen, J.-G. Liu, J. Wurtz, M. D. Lukin, S.-T. Wang, and H. Pichler, PRX Quantum **4**, 010316 (2023).
- [47] M. Lanthaler, C. Dłaska, K. Ender, and W. Lechner, Phys. Rev. Lett. **130**, 220601 (2023).
- [48] A. Omran, H. Levine, A. Keesling, G. Semeghini, T. T. Wang, S. Ebadi, H. Bernien, A. S. Zibrov, H. Pichler, S. Choi, J. Cui, M. Rossignolo, P. Rembold, S. Montangero, T. Calarco, M. Endres, M. Greiner, V. Vuletić, and M. D. Lukin, Science **365**, 570 (2019).
- [49] G. Bornet, G. Emperauger, C. Chen, F. Machado, S. Chern, L. Leclerc, B. Gély, Y. T. Chew, D. Barredo, T. Lahaye, N. Y. Yao, and A. Browaeys, Phys. Rev. Lett. **132**, 263601 (2024).
- [50] T. Manovitz, S. H. Li, S. Ebadi, R. Samajdar, A. A. Geim, S. J. Evered, D. Bluvstein, H. Zhou, N. U. Köyliüoğlu, J. Feldmeier, P. E. Dolgirev, N. Maskara, M. Kalinowski, S. Sachdev, D. A. Huse, M. Greiner, V. Vuletić, and M. D. Lukin, Quantum coarsening and collective dynamics on a programmable quantum simulator (2024), arXiv:2407.03249 [quant-ph].
- [51] J. Wurtz, P. L. S. Lopes, C. Gorgulla, N. Gemelke, A. Keesling, and S. Wang, arXiv:2205.08500 [quant-ph] (2024).
- [52] See Supplemental Material.
- [53] N. Šibalić, J. D. Pritchard, C. S. Adams, and K. J. Weatherill, Comp. Phys. Comm. **220**, 319 (2017).
- [54] D. Kim, A. Keesling, A. Omran, H. Levine, H. Bernien, M. Greiner, M. D. Lukin, and D. R. Englund, Opt. Lett. **44**, 3178 (2019).
- [55] S. Zhang, F. Robicheaux, and M. Saffman, Phys. Rev. A **84**, 043408 (2011).
- [56] T. M. Graham, M. Kwon, B. Grinkemeyer, Z. Marra, X. Jiang, M. T. Lichtman, Y. Sun, M. Ebert, and M. Saffman, Phys. Rev. Lett. **123**, 230501 (2019).
- [57] P. Schroff, A. La Rooij, E. Haller, and S. Kuhr, Scientific Reports **13**, 3252 (2023).
- [58] B. F. Schiffer, D. S. Wild, N. Maskara, M. Cain, M. D. Lukin, and R. Samajdar, Phys. Rev. Res. **6**, 013271 (2024).
- [59] DOI to be added in proof.
- [60] Y. R. P. Sortais, H. Marion, C. Tuchendler, A. M. Lance, M. Lamare, P. Fournet, C. Armellin, R. Mercier, G. Messin, A. Browaeys, and P. Grangier, Phys. Rev. A **75**, 013406 (2007).
- [61] S. de Léséleuc, D. Barredo, V. Lienhard, A. Browaeys, and T. Lahaye, Phys. Rev. A **97**, 053803 (2018).
- [62] R. Legaie, C. J. Picken, and J. D. Pritchard, J. Opt. Soc. Am. B **35**, 892 (2018).
- [63] T. Preuschoff, M. Schlosser, and G. Birkl, Rev. Sci. Inst. **91**, 083001 (2020).
- [64] P. B. Wigley, P. J. Everitt, A. van den Hengel, J. W. Bastian, M. A. Sooriyabandara, G. D. McDonald, K. S. Hardman, C. D. Quinlivan, P. Manju, C. C. N. Kuhn, I. R. Petersen, A. N. Luiten, J. J. Hope, N. P. Robins, and M. R. Hush, Scientific Reports **6**, 25890 (2016).

## Supplemental Material for Demonstration of weighted graph optimization on a Rydberg atom array using local light-shifts

### EXPERIMENT SETUP

#### Neutral Atom Arrays

A schematic of the experimental setup is shown in Fig. 6(a), based on the setup previously introduced in Ref. [20]. Atom arrays are created by loading individual Cs atoms into 1064 nm optical tweezers generated using a spatial light modulator (SLM). Traps are focused to a  $1/e^2$  waist of  $1.5 \mu\text{m}$  using an in-vacuum aspheric lens with  $\text{NA}=0.45$  [60] which has an ITO coating to suppress charge build up. This same lens is used for qubit readout by performing fluorescence imaging with an sCMOS (Teledyne Photometrics Prime BSI) camera.

Following stochastic loading of the array, we rearrange the atoms into the target spatial configuration with a mobile tweezer beam at 1039 nm created using a dual-axis acousto-optic deflector (AOD) driven by a fast micro-controller. Atom sorting is performed using a trap depth of 1 mK and a tweezer of 9.8 mK, using a customised algorithm to calculate moves in real time that aims to minimise the number of atoms movements required to fill the target array sites. We achieve single move efficiencies  $\geq 97\%$ , and typical success rates  $\geq 70\%$  for the graphs shown above using a single round of sorting. For larger graphs, multiple sorting iterations can be performed.

After rearrangement, atoms are optically pumped into the  $|4, 0\rangle$  hyperfine state using  $\pi$ -polarized light on the Cs  $D_1$

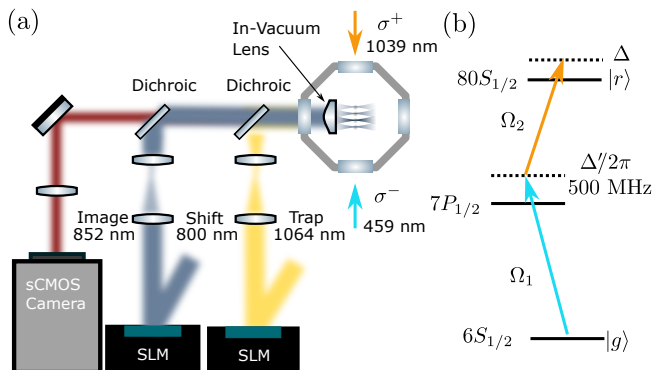


FIG. 6. Experimental Setup. (a) Atom arrays are generated using 1064 nm trapping light projected into the chamber using an SLM and a high-numerical aperture in-vacuum aspheric lens. Local light-shifts are implemented using a second SLM to overlap spots at 800 nm with the 1064 nm tweezers. Atom imaging is performed by collecting fluorescence onto an sCMOS camera. Rydberg excitation is performed using counter-propagating beams at 459 nm and 1039 nm with orthogonal circular polarisations which globally illuminate the array. (b) Two-photon Rydberg excitation scheme from the  $6S_{1/2}$  clock state  $|g\rangle = |4, 0\rangle$  to  $|r\rangle = |ns_{1/2}, m_j = +1/2\rangle$  via the intermediate  $7P_{1/2}$  level. Lasers are locked with a detuning of  $\Delta'/2\pi = 506$  MHz from the  $7P_{1/2}$  transition.

transition resonant with the  $F = 4 \rightarrow F' = 4$ , achieving an optical pumping efficiency of  $0.971(9)$  measured using microwave benchmarking [20].

For the experiments in this paper, prior to Rydberg operations the optical dipole traps are ramped down to  $15 \mu\text{K}$ , cooling the atoms to temperatures of  $2 \mu\text{K}$ . Atoms are then released for  $5 \mu\text{s}$  to minimise the mechanical force of the tweezer beams on the Rydberg states, and atoms are then recaptured at 1 mK to facilitate efficient Rydberg state detection [61].

#### Rydberg Excitation

Rydberg excitation is performed using two-photon excitation via the intermediate excited state as shown in Fig. 6(b) using light at 459 nm and 1039 nm to drive transitions from  $6P_{1/2} \rightarrow 7P_{1/2}$  and  $7P_{1/2} \rightarrow ns_{1/2}$  respectively. Both beams are derived from Ti:Sapph lasers (M Squared Sol-SiS) at 918 nm and 1039 nm which are frequency stabilised to a commercial ULE cavity (M Squared) offering finesse  $\mathcal{F} > 40$  k at both wavelengths. The lasers are offset-locked using a Pound-Drever-Hall with fiber EOMs [62] to provide controllable detuning with respect to the 3 GHz spaced cavity modes, with few kHz linewidths measured via a beatnote between the two lasers.

The 459 nm light is frequency doubled (M Squared ECDF) and the detuning controlled using a double pass acousto-optic modulator (AOM, AA MQ180-A0.25-VIS) in a cat-eye geometry to enable fast frequency control. The AOM is driven using a high bandwidth arbitrary waveform generator (AWG, Spectrum M4i6631-x8). This is delivered to the experiment by fiber, and overlapped onto the array with a  $125 \mu\text{m}$   $1/e^2$  waist. The 1039 nm laser seeds a fiber amplifier (Azur ALS-1039-20-CP) which is intensity controlled using a single-pass AOM and coupled into a high-power fiber. The beam is then imaged onto the atoms using cylindrical optics to create a beam with a  $1/e^2$  waist size of  $60 \times 20 \mu\text{m}$ . For the experiments presented here, Rydberg excitation is performed using an intermediate detuning of  $\Delta'/2\pi = 506$  MHz with respect to the  $7P_{1/2}$  centre of mass energy, with powers set to provide a Rabi frequency of  $\Omega/2\pi = 2.70(0)$  MHz over the central rows of the array.

To stabilise the intensity, prior to each experimental cycle a 1 ms sample pulse is applied allowing closed-loop feedback to an AOM based noise eater on each laser [63], with the intensity held constant for the fast Rydberg pulses. We achieve 1% shot-to-shot stability stable over hours using this technique.



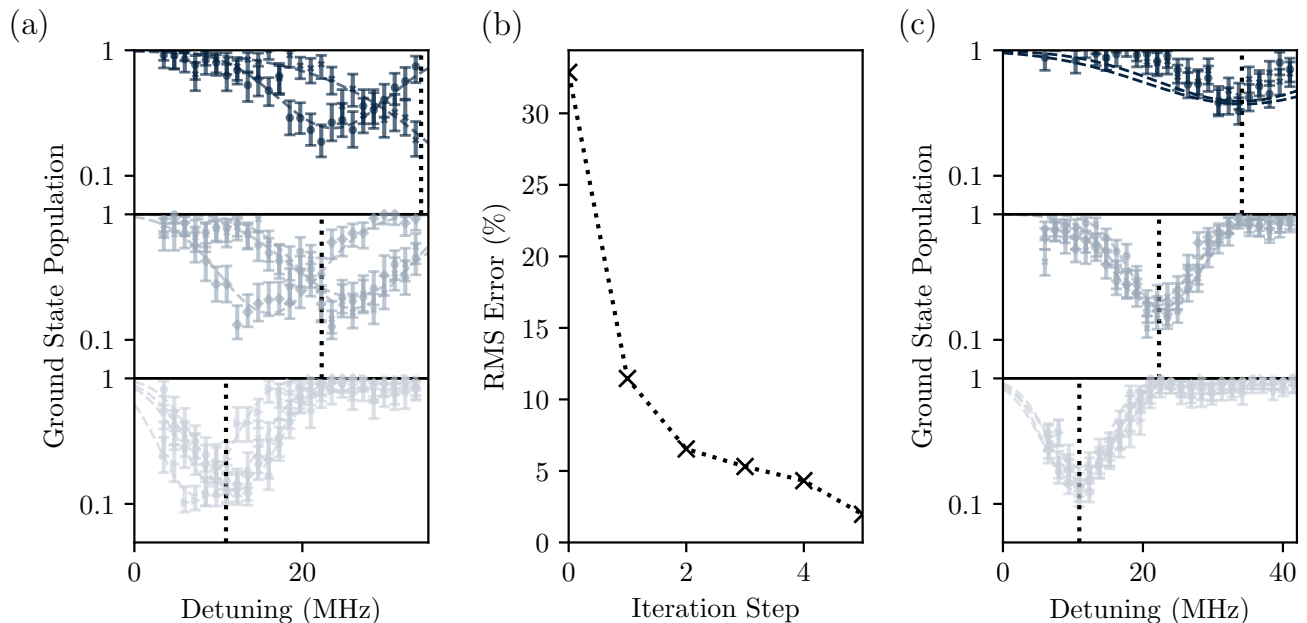


FIG. 7. Feedback on local light-shift potentials. (a) Spectroscopy of initial hologram generation for the  $3 \times 3$  atom arrangement with  $(w_1, w_2, w_3, w_4, w_5) = (1, 2, 1, 2, 2)$  requiring  $w_\alpha = 2$  and  $w_\beta = 3$  shows significant variation in the shift experienced by each atom. (b) Performing closed-loop feedback on the SLM hologram generation using the measured light shifts enables rapid convergence onto the target light shifts with RMS below  $< 2\%$ . (c) Spectroscopy measurement performed after iteration 5 showing close convergence of the relative shifts experienced by each atom. The dashed line shows the targeted resonance for each atom.

### Local Light-shifts

To apply local light-shifts for implementing graph weighting, an 800 nm laser (M Squared SolsTiS) is used with a second spatial light modulator to create a secondary tweezer array that is overlapped with the underlying 1064 nm traps as shown in Fig. 6(a). Due to the chromatic shifts of the in-vacuum aspheric, it is not possible to image both 1064 nm and 800 nm arrays overlapped after the chamber focused in a common plane. Instead, to overlap the arrays we exploit the fact that ground-state atoms are anti-trapped by this blue detuned light. Using this effect, we initially generate arrays with a  $2 \mu\text{m}$  waist and apply the 800 nm potential onto the trapped atoms for 1-10 ms, resulting in ejection of atoms from sites that are overlapped between the two beams. Using  $10 \times 10$  arrays with  $8 \mu\text{m}$  spacing, we perform multiple iterations to adjust relative spacing, rotation and defocus of the 800 spots with respect to the 1064 nm array using the SLM to maximise the relative alignment of the two arrays by minimising atom survival. This also ensures the 800 nm light is focused on the same plane as the 1064 nm traps.

For performing local-light shifts, we suppress the mechanical effects of the repulsive light shift on the ground-state atoms by changing the input beam size on the SLM to create spots with an effective waist size of  $3.0(4) \mu\text{m}$ , resulting in  $< 2\%$  additional atom loss when applying local shifts of up to 10 MHz for periods of up to  $3 \mu\text{s}$ .

Light-shift potentials are generated using the Gerchberg-Saxton algorithm [54], with the modification that the relative weighting of each spot is adjusted to reflect the target weighting  $w_i$  of the specific graph problem. Following the initial hologram generation, we perform Rydberg spectroscopy at  $n = 50$  to minimise shifts due to interactions to measure the resulting  $\delta_{AC}^i$  for each site. An example spectroscopy measurement is shown in Fig. 7(a) for the case of the  $(w_1, w_2, w_3, w_4, w_5) = (1, 2, 1, 2, 2)$  graph requiring  $w_\alpha = 2$  and  $w_\beta = 3$ . This data shows that whilst sites initially defined with higher weightings have larger shifts, there is a large RMS error between the initial hologram generation and the target light shifts. To rectify this, we implement closed-loop feedback on the relative weightings using the same approach used for normalising relative intensity in trap arrays [29, 54]. Following each spectroscopy measurement, an additional hologram generation step is taken using updated weights to drive convergence towards the target light-shifts. Fig. 7(b) shows this can be used to obtain RMS errors  $< 2\%$  after 5 iterations, with the measured light-shifts after the final iteration shown in Fig. 7(c) highlighting the ability to obtain accurate light shift potentials.

### Weighted-graph Annealing

Optimization of weighted graphs is performed using a dual-stage annealing profile as illustrate in Fig. 1(c). To simplify optimization of the annealing profile, we parameterize the detuning using a cubic ramp of the form [28]

$$\delta(t) = at^3 + bt + c, \quad (3)$$

with ramp parameters  $a = 8sc/\tau^3$ ,  $b = 2c/\tau - a\tau^2/4$  and  $c = (\Delta_{\max} - \Delta_{\min})/2$ . Here  $0 \leq s \leq 1$  acts as a shape parameter, with  $s = 0$  equivalent to a linear ramp, and  $\tau$  is the total ramp duration.

This profile is then used to build piece-wise profiles, with the global Rydberg laser detuning  $\Delta(t)$  and 800 nm light-shift  $\delta_{AC}$  given by

$$\Delta(t) = \begin{cases} \delta(t) & \text{if } \delta(t) < 0, \\ 0 & \text{otherwise,} \end{cases}, \delta_{AC}(t) = \begin{cases} 0 & \text{if } \delta(t) < 0, \\ \delta(t) & \text{otherwise.} \end{cases} \quad (4)$$

To synchronise the pulses, the parameters are sent to the same dual channel AWG with one channel controlling amplitude and frequency of the 459 nm laser, and the second channel connected to the 800 nm AOM situated before the SLM that provides intensity control.

For the graphs shown above, annealing profile parameters  $s$ ,  $\tau$ ,  $\Delta_{\min}$  and  $\Delta_{\max}$  are optimized using MLOOP [64], an open source machine learning package interfaced through Python. For each set of parameters, we perform 200-300 repeated measurements to evaluate the averaged classical cost function  $\langle H_{\text{MWIS}} \rangle$  from the distribution of experimentally observed bitstrings, and use this cost to control the evolution of the optimization process. Following optimization, we perform 1000 shot repeats to verify the final output probabilities presented in the paper.